Thermal conductivity of highly porous metal foams: Experimental and image based finite element analysis

Yasin Amani, Atsushi Takahashi, Patrice Chantrenne, Shigenao Maruyama, Sylvain Dancette, Eric Maire

THERMAL CONDUCTIVITY OF HIGHLY POROUS METAL FOAMS: EXPERIMENTAL AND IMAGE BASED FINITE ELEMENT ANALYSIS

Yasin Amani[a], Atsushi Takahashi[b], Patrice Chantrenne[a,*], Shigenao Maruyama[c], Sylvain Dancette[a], Eric Maire[a]

[a] *INSA de Lyon, MATEIS CNRS UMR5510, Université de Lyon, 69621 Villeurbanne, France*

[b] *Graduate School of Engineering, Tohoku University, 6-6 , Aoba, Aramaki, Aoba-ku, Sendai, Miyagi, 980-8579, Japan*

[c] *Institute of Fluid Science, Tohoku University, 2-1-1, Katahira, Aoba-ku, Sendai, Miyagi 980-8577, Japan*

Abstract

X-ray tomography is used to produce three-dimensional images of an aluminium alloy foam with a high porosity ($> 93\,\%$). These data allow describing the foam structure from which a finite element model is derived to predict the thermal conductivity of the foam. The results are compared with experimental values measured by a new guarded hot plate apparatus adapted for the range of thermal conductivity values of interest. Good agreement is observed which validated the finite element model used to evaluate the thermal properties of any porous metallic foam with stochastic cell size and configuration. Furthermore, the thermal conductivity of the foam has also been predicted using previous analytical models. The differences with previous values show that it is important to account for the real geometry of

*Corresponding author. Tel.: +33 (0) 47 243 6155

Email address: patrice.chantrenne@insa-lyon.fr (Patrice Chantrenne)

Preprint submitted to International Journal of Heat and Mass Transfer January 11, 2018

the foam to get an accurate value of the thermal conductivity.

Keywords: Image analysis, 3-D modeling, Numerical simulation, Measurement, Open-cell foam, Conduction

---

1. Introduction

Manufacturing technologies produce new types of porous materials which are widely used as key elements where low Thermal Conductivity (TC) is required. Therefore, they are mostly applied for refrigeration [1], thermal energy storage [2] and insulation [3] purposes. They divide into closed-cell and open-cell types based on their morphologies. For each cell type, the structure might be stochastic or periodic. Open-cell foams normally have higher TC than closed-cell foams of similar densities due to bigger cell sizes and disclosed gas volume which causes convection [4].

In the case of open-cell foams, the architecture and material of the foam skeleton influence TC. Bhattacharya et al. [5] mentioned that the value of TC depends strongly on the foam porosity and the configuration of struts and their intersections. Afterwards, Singh and Kasana [6] stated that TC relies on the ratio of the TC of the constituents as well. Peak et al. [7] mentioned that TC increases as the porosity decreases. However, it varies little by changing the cell size at fixed porosity.

Heat transfer mechanism through a foam is a consequence of conduction in the solid phase, conduction and convection in the gaseous phase and thermal radiation. The contribution of each heat transfer mechanism is a key factor when the TC is supposed to be set to a desired value while keeping

the porosity fixed. Calmidi and Mahajan [8] remarked that at low temperatures, (between 333 and 348 K) nonlinear effects such as natural convection and radiation are negligible. However, at higher temperatures, they have a significant influence on TC [9, 10, 11, 12, 13]. In this paper, we focus on the prediction of the solid phase contribution to TC. The studied foam is a 40 PPI (Pores Per Inch) Duocel® open-cell foam produced by ERG Aerospace Corporation depicted in Figure 1. The samples are made of 6101 aluminium alloy subjected to a T6 precipitation-hardening heat treatment. The prediction and measurements are done in two conditions: first the foam with air and secondly the foam embedded in epoxy resin. The densities and TC of aluminium, air and epoxy resin are given in Table 1. These parameters do not vary significantly within the temperature ranges considered in this study. Thus, they are assumed to be constant. For the first configuration, it has been shown that the convective and radiative heat transfer are negligible as compared to conduction heat transfer. For the second configuration, the convective and radiative heat transfers are suppressed. So, the experimental and predicted values might be directly compared.

The geometry of the foam is determined using X-ray tomography (section 2). The measurement methodology is detailed in section 3. From the geometry obtained by X-ray tomography, a Finite Element (FE) analysis is

Table 1: TC and densities of foam components.

Material	Density ($kg \cdot m^{-3}$)	TC ($W \cdot m^{-1} \cdot K^{-1}$)
6101-T6	2700 [14]	218 [15]
Epoxy resin	1147	0.1813
Air (305 K, 1 atm)	1.1839	0.0265

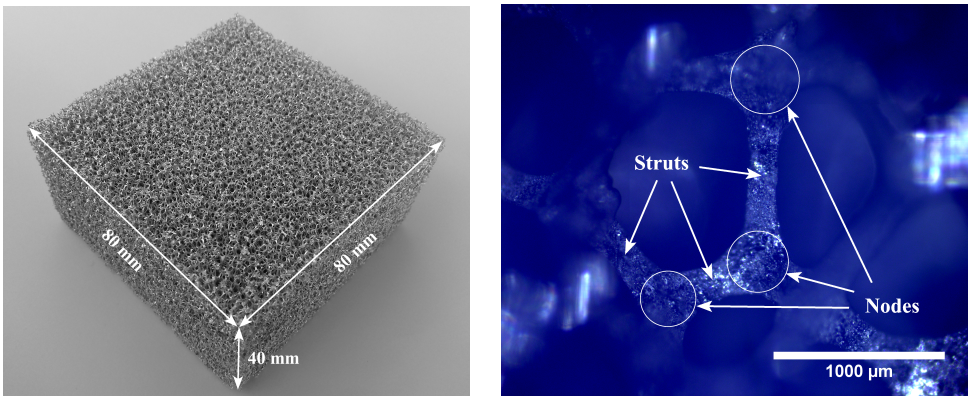

(a) (b)

Figure 1: (a) Open-cell aluminium alloy foam with a porosity of $\varepsilon = 0.927$. (b) Close-up view of a single cell of the foam via optical microscopy.

conducted to predict the conduction part of TC (section 4). Also, the X-ray tomography images are used to extract the geometrical characteristics to evaluate the conduction part of TC using analytical models (section 5). The results are compared in the last section.

2. Tomography

The architecture of the foam block is obtained by X-ray tomography [16, 17]. It relies on the Beer-Lambert law which implies that every line integral of the attenuation coefficient along the X-ray beam path corresponds to an object in the recorded projection [18]. The result is a Two-Dimensional (2-D) image of a Three-Dimensional (3-D) object projected on the detector screen. In order to obtain the 3-D structure, the sample is rotated in 720 steps between $0\,^\circ$ and $360\,^\circ$ and an average of three images is taken at each step. Then, a standard filtered back-projection algorithm is used to reconstruct

the final 3-D image.

The best resolution that can be obtained by global tomography depends on the dimensions of the sample and the size of the detector. Several tricks are played to scan the whole samples that are 80 mm × 80 mm × 40 mm. The distance between the detector and the X-ray tube shown in Figure 2(a) is fixed. The sample can be displaced in x direction and the closer to the X-ray tube results in the better resolution obtained by the detector. In a common tomography procedure, the detector is fixed in front of the X-ray tube and the sample should be placed at distance x_1 away from the detector. However the resolution obtained using this technique is 46 μm, which is not enough in this study. Therefore, another method called "double detector" or "stitching" tomography is used. In this method, the detector is displaced in the y direction which expands the cone beam volume recorded. The sample can then be placed at distance x_2, closer to the X-ray tube, which provides a 23 μm resolution. Also, the sample is displaced in the z direction to be scanned locally step by step as illustrated in Figure 2(b). The X-ray tube operates at an acceleration voltage of 80 kV using a tungsten transmission target with a 280 μA current. The spot size is between 2-3 μm during all scans.

Nodes and struts of the foam are analysed in the 3-D image using the Fiji software to evaluate node-to-node distance and average node and strut thicknesses (Table 3). In order to evaluate node-to-node distance distribution, voxels from the edges of the solid phase in the binary 3-D image are removed using the Binary-Erode plugin of Fiji. Voxels of struts are removed

entirely while some voxels of nodes remain by repeating the erosion procedure because the average node thickness is higher than that of the struts. The clusters of voxels are labelled by giving them different colours. An in-house plugin is used to compute node-to-node distances. This plugin computes all minimum distances between pairs of labelled objects.

The solid phase is analysed using the local thickness plugin of Fiji. The plugin estimates the local thickness by the largest sphere that fits in the solid phase and contains its voxels. The result of the analysis is a 3-D stack of the foam structure with different colours corresponding to different local thicknesses. The histogram plot of colours in such 3-D image illustrating the number of voxels against local thickness has two peaks, the average strut diameter and the average node diameter respectively.

The average and distribution of void-cells in three directions are evaluated by analysis of the gaseous phase of the 3-D binary image using a 3-D Watershed plugin implemented in Fiji. This plugin splits the continuous gaseous phase into void cells without overlapping and gives them different labels. These segmented void cells do not contain any strut or node. One slice in the resulting labellized volume is illustrated in Figure 3. The so-called "Feret" diameter of each segmented cell can be evaluated by another in-house plugin from the minimum and maximum x, y and z values of its voxels.

Furthermore, the average diameter D_i ($i = x,\ y,\ z$) of void-cells is calculated in x, y and z directions and their probability distribution functions are plotted in Figure 4. These functions can be fitted by normal distribution

functions, resulting in the values given in Table 3. The average diameter of void-cells is bigger in the z direction, corresponding to the rolling direction.

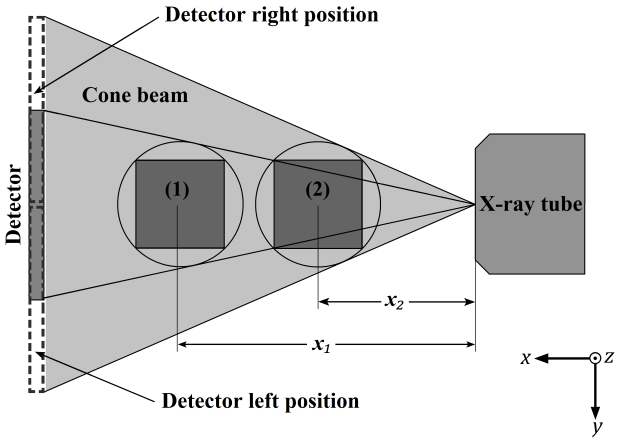

(a)

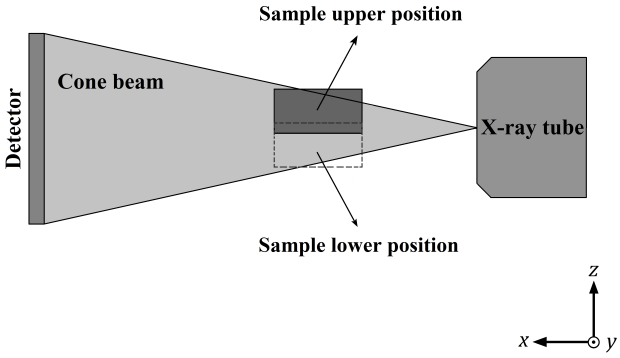

(b)

Figure 2: Schematic illustration of X-ray tomography from (a) top and (b) side views.

3. Experimental Approach

3.1. Experimental Set-up

TC is measured using the guarded hot plate principle. Figure 5 shows a schematic illustration of the developed Guarded Hot Plate Apparatus (GHPA), utilising Peltier modules. This apparatus consists of the specimen, cold plate, hot plate, surrounding thermal insulation materials and several electrical devices. The cold plate and guard plate present a penny shape. The cold plate is made of pure aluminium ($k = 228\,\mathrm{W{\cdot}m^{-1}{\cdot}K^{-1}}$). A Negative Temperature Coefficient (NTC) thermistor is settled in the centre of the plate surface to measure surface temperature using a digital multimeter. Two Peltier modules are also put into the hot and cold plates to maintain the temperature at the target value. A water cooling bath is set on the cold plate to remove exhaust heat from the Peltier module. Both the guard and the main plates are made of pure copper. A silicone rubber heater is rolled around the guard plate to be used as the guard heater. A precise foil resistor is placed on top of the hot plate as the main heater. Loading voltages of the Peltier module, the guard heater and the main heater are regulated

Table 2: Dimensions of the samples used in this study.

Sample No.	Configuration	Width (mm)	Length (mm)	Depth (mm)
1	Foam-air	79.79 ± 0.39	79.91 ± 0.43	09.75 ± 0.44
2	Foam-air	79.93 ± 0.18	79.94 ± 0.24	20.03 ± 0.19
3	Foam-air	80.03 ± 0.09	80.15 ± 0.31	30.00 ± 0.18
4	Foam-air	79.79 ± 0.95	79.89 ± 0.85	39.98 ± 0.44
5	Foam-resin	79.88 ± 0.33	79.97 ± 0.49	09.36 ± 0.10
6	Foam-resin	79.21 ± 0.35	79.42 ± 0.51	19.05 ± 0.10
7	Foam-resin	79.37 ± 0.62	79.49 ± 0.25	29.33 ± 0.16
8	Foam-resin	78.91 ± 0.33	79.06 ± 0.06	39.32 ± 0.11

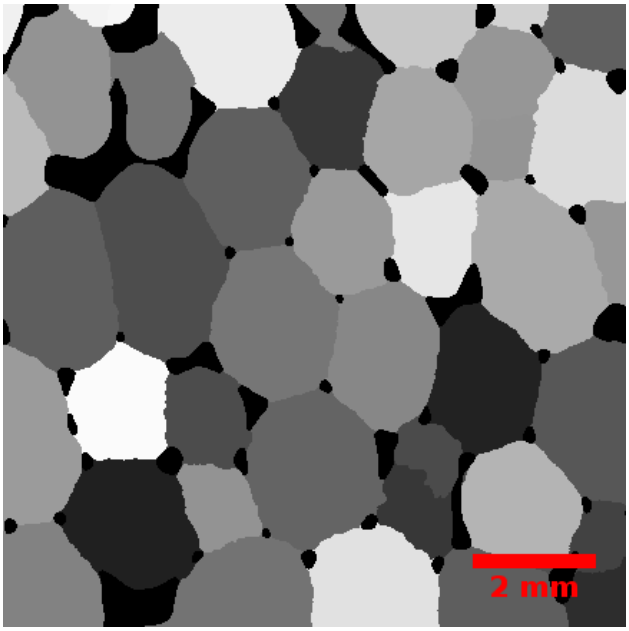

Figure 3: One slice of the 3D stack with labelized segmented void-cells generated by the 3D watershed plugin. The plugin works with two parameters called inspect radius and expand radius, both set equal to 5.

by the power supply. The Peltier module installed between the hot and guard plates measures the temperature difference. All components are surrounded by thermal insulation material to decrease heat loss from the GHPA. The temperature difference between hot and guard plates can be controlled within $\pm 0.02\,\mathrm{mK}$, which is higher than the sensitivity of the thermocouple. This allows generating a uni-dimensional temperature gradient in the heat transfer area and a precise measurement of TC.

It lasts between one and two hours for the testing devices to stabilise under steady state condition depending on the sample thickness and thermal properties. The hot and cold plate temperature evolutions with time are

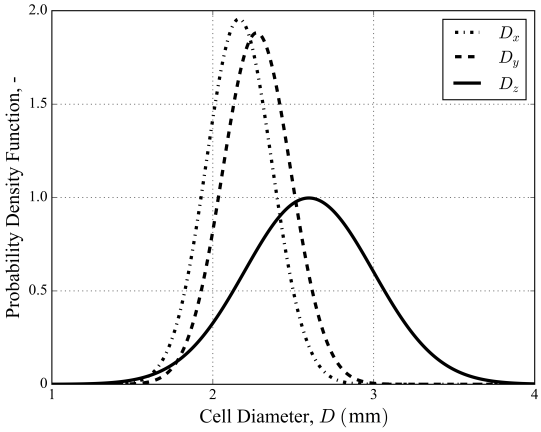

Figure 4: Normal distributions of pore diameters in x, y and z directions.

plotted in Figure 6(a). The diagram of temperature difference in the Peltier module as a function of time is depicted in Figure 6(b).

The cold and hot plate temperatures are set to the target temperatures with 1 mK and 22 mK fluctuations respectively. Furthermore, temperature difference fluctuation measured by the Peltier module shall be fixed to the value below 0.1 mK. The temperature difference of the stabilised system with the Peltier module fluctuates approximately 100 times less than that of the thermocouple [19, 20]. Thus, heat transfer in the lateral directions is

Table 3: Geometrical characteristics of the studied foam.

	Average (mm)	Standard deviation (mm)
Strut thickness $2t$	0.188	0.001
Node thickness $2b$	0.293	0.001
Void-cell diameter in x	2.163	0.204
Void-cell diameter in y	2.273	0.212
Void-cell diameter in z	2.597	0.400
Node-to-node distance L	1.538	0.433

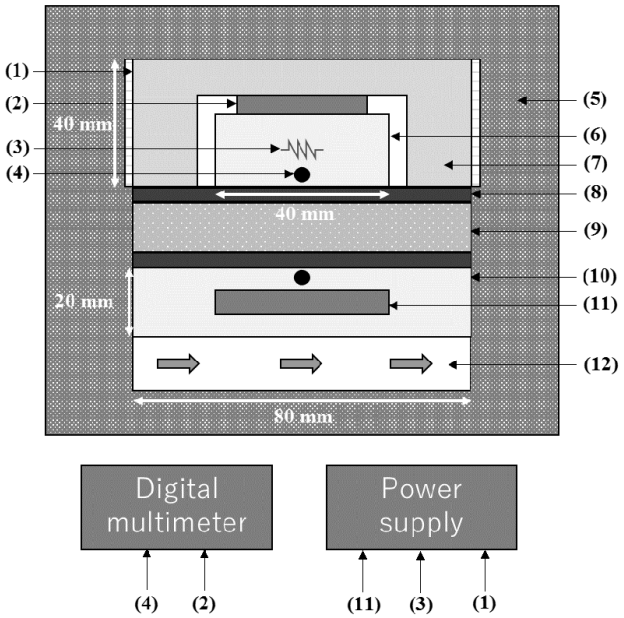

Figure 5: Sketch of the measurement system: (1) guard heater (silicone rubber heater), (2) Peltier module, (3) main heater, (4) NTC thermistor, (5) polystyrene foam, (6) hot plate (Cu), (7) guard plate (Cu), (8) silicone pad, (9) foam sample, (10) cold plate, (11) Peltier module, (12) cooling water flow.

negligible which implies one-dimensional vertical heat transfer through the specimen.

3.2. Methodology

Two Peltier modules inside the cold and hot plates are set so that the temperature difference between hot and cold plates becomes $\Delta T = 10\,\mathrm{K}$ for aluminium foam with air and $\Delta T = 5\,\mathrm{K}$ for aluminium foam embedded in the epoxy resin. In addition, the power of the main heater in the hot plate is adjusted so that the temperature difference between the hot and guard plate detected by the Peltier module becomes $0\,\mathrm{K}$. In steady state condition, the

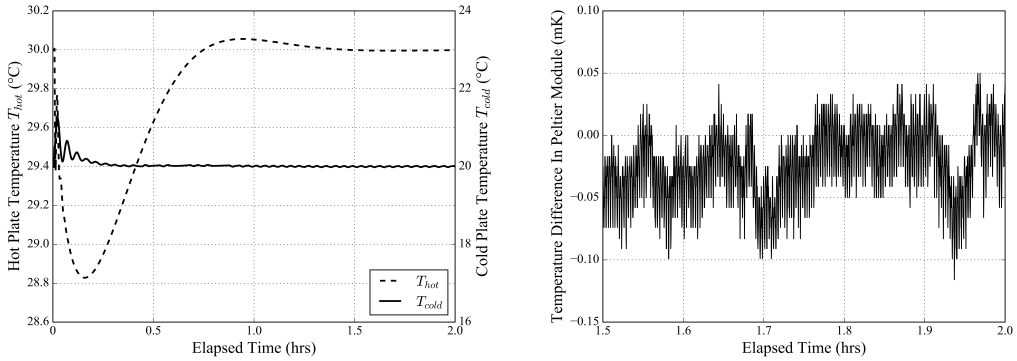

(a) (b)

Figure 6: (a) Hot and cold plate temperatures and (b) temperature difference in Peltier module as a function of time.

heat transferred from the hot plate to the cold plate, Q, equals to the heat power dissipated in the main heater of the hot plate and is proportional to the temperature difference ΔT.

$$\Delta T = \frac{R.Q}{A} \tag{1}$$

where R is the total thermal resistance between the hot and cold plates and A is defined as the cross-section area of the hot plate. The latter exhibits a penny shape with a diameter equal to 28 mm and 30 mm for the experiments concerning samples with air and embedded in epoxy resin respectively.

A preliminary study has shown that when the foam is in direct contact with the hot and cold plates, the thermal contact resistance is much higher than the sample thermal resistance; it is then difficult to extract the thermal resistance of the sample [8, 20, 21] with high accuracy. Consequently, two

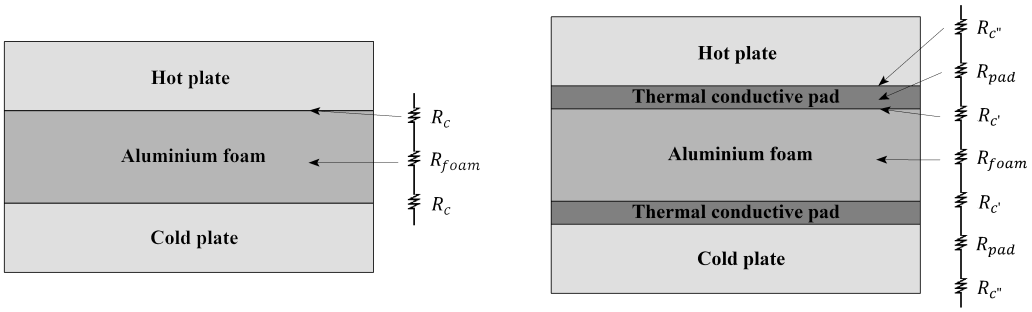

(a) (b)

Figure 7: Equivalent thermal circuits of the aluminium foam (a) without and (b) with silicone pads.

5 mm thick silicone pads are installed between the specimen and the plates to reduce thermal contact resistances. The total thermal resistance is evaluated by a thermal-electrical analogy [22]. It consists in summing the thermal resistances of pads, R_{pad}, the thermal contact resistances, $R_{c'}$ and $R_{c''}$, and the thermal resistance of the aluminium foam R_{foam} (Figure 7(a) and (b)). Therefore, the total thermal resistance is expressed as:

$$R = R_{foam} + 2(R_{pad} + R_{c'} + R_{c''}) \tag{2}$$

If heat is transferred only by conduction in the foam sample, then the thermal resistance of the foam R_{foam} is equal to:

$$R_{foam} = \frac{t_{foam}}{\lambda_{foam}} \tag{3}$$

where t_{foam} is the thickness of the foam sample. Different measurements have been done varying the pressure between the cold and hot plates. When

the pressure is high enough, $2(R_{pad} + R_{c'} + R_{c''})$ converges to a constant value. Then the thermal resistance between the plates depends linearly on the sample thickness.

$$R = \frac{t_{foam}}{\lambda_{foam}} + 2(R_{pad} + R_{c'} + R_{c''}) \tag{4}$$

Therefore, λ_{foam} is evaluated from the slope of the $R - t_{foam}$ curve, which is determined by measuring the thermal resistance R for samples with different thicknesses.

From Eq. 1 the uncertainty of the measured R can be estimated as following equation:

$$U = k_{cf}\sqrt{\sum_{i=1}^{n}(c_i^2 u_i^2)}, c_i = \frac{\partial R}{\partial \eta_i} \tag{5}$$

where U is the expanded uncertainty with a coverage factor $k_{cf} = 2$, which provides an interval with a level of confidence of approximately 95 %. u_i and c_i are the standard uncertainty and sensitivity coefficients of variable η_i, respectively. The variables (heat transfer area of the main plate A, heat power Q and the temperature difference between two plates ΔT) were considered as η_i to estimate the measurement expanded uncertainty. The expanded uncertainty of the thermal resistance was evaluated to be in the range of 1.6-2.0 %.

3.3. Results

Eight samples were used for TC measurement, with the sizes listed in 2. Four samples in air and four samples embedded in epoxy resin were used. In

order to minimise the influence of natural convection when the foam with air is characterised, the hot and cold plates are placed on the top and bottom of specimens respectively.

The thermal resistance of the foam varies linearly with the thickness. Consequently, the foam TC is independent of its thickness. It means that the foam thicknesses chosen for TC measurements are large enough to consider the foam as a homogeneous material. In addition, the aluminium phase TC remains constant around ambient temperature.

For the foam embedded in epoxy resin, convective heat transfer does not exist and radiative heat transfer is negligible as compared to conduction heat transfer since the solid phases are opaque. Hence, the measured TC is due to conduction heat transfer in both phases (aluminium and resin).

For the aluminium foam sample in air, air conduction heat transfer is negligible even if the porosity is around 0.93 since the ratio between the TC of aluminium and air is about 10000. Moreover, as the hot plate is above the cold plate and the temperature between these two plates is equal to 10 °C, considering the pore size (around 2 mm) and the air thermal properties, the Rayleigh number ($Re = 16.55$) is not high enough to allow the development of convection cells. Radiative equivalent TC in the foam with air can be expressed by a diffuse approximation that depends on the average cubic temperature of the sample [23, 24]. The TC of the foam exhibits a constant response to increasing T^{-3} (Figure 8) when the temperature level varies between 20 °C and 34 °C. Thus, the radiative contribution to heat transfer is then assumed to be negligible compared to the conduction heat transfer. This

is coherent with previous measurements which led to the conclusion that the radiative heat transfer is negligible for the foam at temperature levels lower than 75 °C [8].

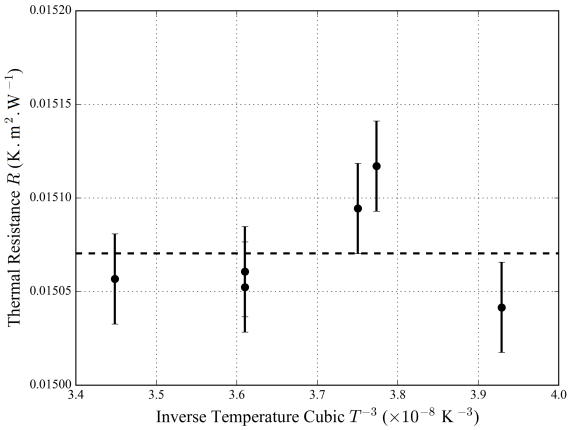

Figure 8: Effect of thermal radiation on the measured thermal resistance of the foam sample.

Figure 9 depicts the thermal resistances of aluminium foams with various thicknesses with air and embedded in the epoxy resin, as measured for evaluating the TC. The approximate line is obtained using the least-square method. The y-intercept of the approximate line is assumed to be the summation of contact and silicone pads thermal resistances. The TC of the foam sample in the z direction is determined using the slope of a line based on Eq. 4. The resulting values of TC are 4.65 $\pm$ 0.41 W·m^{-1}·K^{-1} and 5.70 $\pm$ 1.78 W·m^{-1}·K^{-1} for the foam with air and embedded in the epoxy resin respectively. The uncertainty of TC of the aluminium foam with air is less than that embedded in the epoxy resin due to the better surface condition.

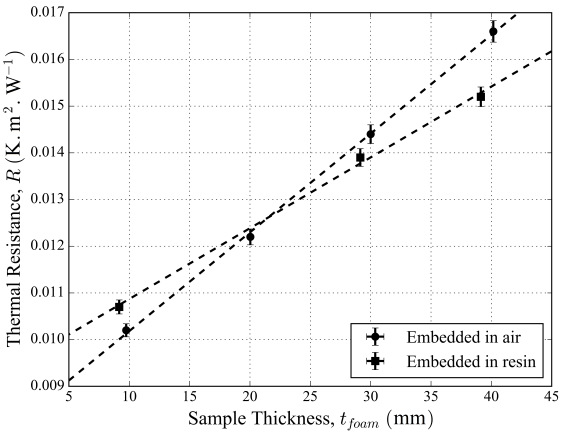

Figure 9: Measured thermal resistance between hot and cold plates as a function of foam sample thickness.

4. Finite Element Analysis

The aim of the FE analysis is to estimate the conduction part of the foam TC based on its geometry obtained by X-ray tomography. The X-ray tomography volume is meshed with continuum finite elements [25, 26]. TC is predicted by simulating a guarded hot plate experiment with the ABAQUS software [27]. A temperature difference is applied between the two parallel sides of the sample perpendicular to the direction in which the TC is to be predicted. The steady state computed temperature profile is shown in Figure 10. It allows the determination of the heat flux across the sample between the hot and the cold surfaces. TC is calculated using the Fourier's Law. In the case of the foam with air and the foam embedded in the epoxy resin, the simulation is conducted only through the metallic phase and the metallic + epoxy phases, respectively.

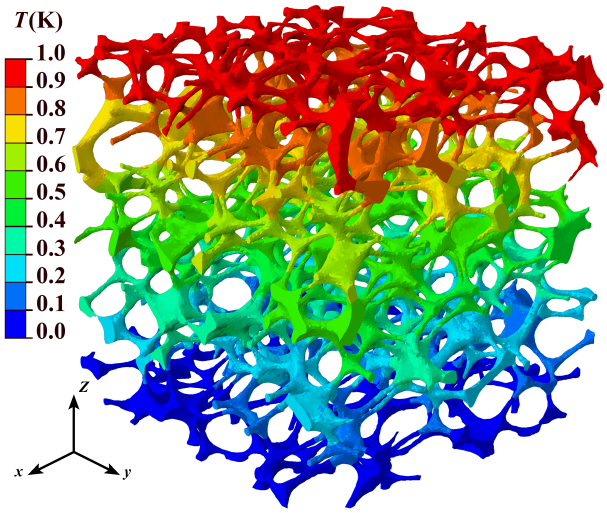

Figure 10: Temperature contour plot computed by FE simulation based on Fourier's law.

The simulation of the whole 3-D volume of real samples with the dimension of 80 mm × 80 mm × 40 mm requires a computer equipped with large memory and is time-consuming. So the minimum representative volume size should be determined to prevent edge effect due to the sample inhomogeneity. Figure 12 shows the variation of TC as a function of volume size. Each volume considered here is meshed with an identical characteristic element size of 88.8 μm. The difference between the resulting values of TC for the volume with 15 mm × 15 mm × 15 mm and 10 mm × 10 mm × 10 mm is less than 1 %. As a compromise between computational time and accuracy of the resulting TC, a minimum representative volume size of 10 mm × 10 mm × 10 mm is chosen. This is comparable with previous results suggesting at least seven [28] and five [29] void-cells in the testing direction.

Afterwards, five 3-D images with the representative volume size are cropped

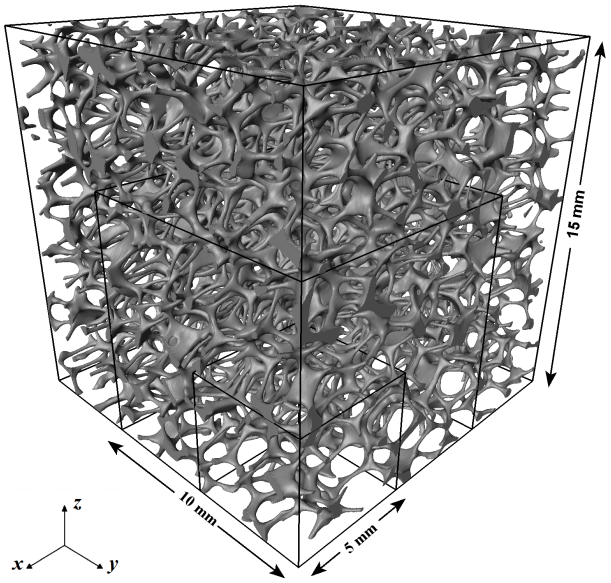

Figure 11: Three volumes with different sizes used to check the edge effect on the resulting values of TC in FE simulations .

randomly from different spots of the entire stack. The tomographic image contains an unclear border changing from black to grey levels between the two phases of the foam. In order to investigate the effect of the solid phase thresholding on the resulting TC, every 3-D image is thresholded to get the average, lower bound and upper bound values (0.927, 0.927 - 0.001 and 0.927 + 0.001) of the porosity which has been previously determined. The porosity is defined as the volume of the aluminium phase divided by the total volume of the foam. The value is calculated by dividing the density of the foam in air by the density of bulk aluminium.

All 15 images are analysed with the commercial Avizo® software [30] to define the surface mesh of the foam with 3-node triangles. The surface mesh

can be simplified and optimized to reduce the number of triangles while preserving a good description of the surface. Finally, the volume mesh is generated automatically from the closed surface mesh using the frontal tetrahedral meshing algorithm of Avizo. The procedure was described initially in Youssef et al. [31]. The resulting 3-D mesh is finally exported to second order thermal tetrahedra (DC3D10) in the ABAQUS commercial software [27].

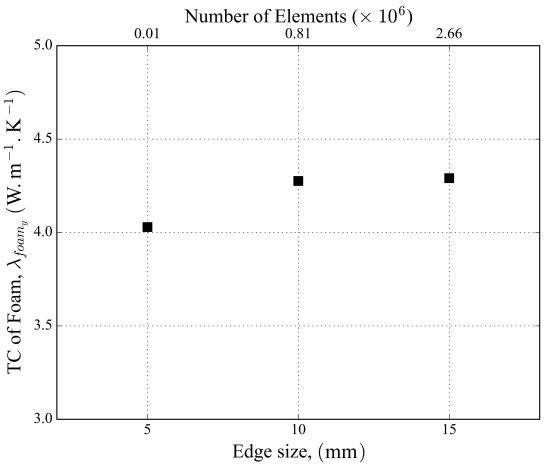

Figure 12: Variation of TC as a function of volume size. The three volumes (shown in Figure 11) are meshed with a characteristic element size of 88.8 μm.

Figure 13 shows the effect of characteristic element size on the resulting value of TC. As the computation time increases exponentially with the number of elements [32], a compromise between computation time and accuracy should be found. According to Figure 13, the element size should be smaller than 5.33×10^{-5} m. TC was calculated in the x, y, and z directions. The converged value of TC in the z direction is higher than those in x and y directions, revealing the anisotropy of TC inherited from the rolling process.

The average strut thickness is 188 μm in the volume, while the average tetrahedron size is 50 μm based on the above mesh convergence study. This means that at least three tetrahedra are present across the thickness of the foam struts. Moreover, the generated 3-D volumes are systematically inspected visually to ensure that the mesh is sufficiently fine to describe the actual architecture properly. The mesh convergence study of Figure 13 also illustrates the fact that decreasing the size of the tetrahedra below 50 μm does not affect the resulting value of the calculated TC significantly.

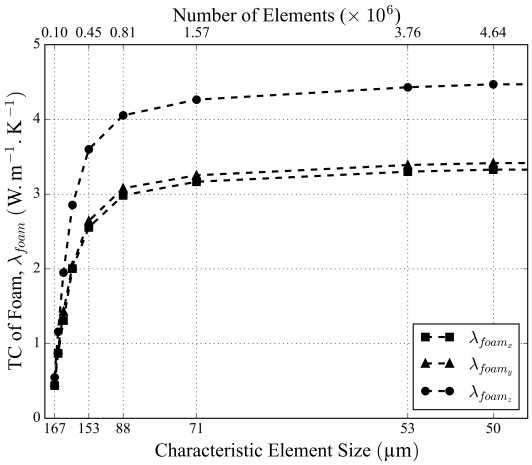

Figure 13: Mesh convergence of the computed foam TC in x, y and z directions.

The average value of computed TC and uncertainty are calculated for every three series of five images with different porosities. They are evaluated according to formulas from the theory of error propagation. Resulting values of TC are listed in Table 4.

5. Analytical Models

Semi-analytical models have been developed in the literature to predict the conduction part of TC in open-cell ERG aluminium foam with porosity values ranging between $0.9 \sim 0.98$ [8, 20, 33, 34, 35, 36]. In these models, the equations determining the TC of the foam have been derived using the thermal-electrical analogy to calculate the thermal resistance of the foam modelled either by a hexagon in 2-D or by a tetrakaidecahedron in 3-D models. These models require the knowledge of geometrical parameters which may be determined by the analysis of the geometry obtained from X-ray tomography. However, due to the difference between the real geometry and the models, the results may not match the experimental values. Previous authors fitted some parameters to get results in closer agreement with experiments.

Five analytical models are presented below, giving the formulae of the foam TC as a function of aluminium TC, λ_s, the other phase TC (air or epoxy resin in our case), λ_f, and the geometrical parameters.

Clamidi and Mahajan [8] proposed a 2-D hexagonal structure consisting of square nodes linked by struts (Figure 14(a)). The formula for the TC of the foam equals:

Table 4: Values of TC obtained by FE simulations in x, y and z directions.

Configuration	$\lambda_{foam_x} = (\mathrm{W{\cdot}m^{-1}{\cdot}K^{-1}})$	$\lambda_{foam_y} = (\mathrm{W{\cdot}m^{-1}{\cdot}K^{-1}})$	$\lambda_{foam_z} = (\mathrm{W{\cdot}m^{-1}{\cdot}K^{-1}})$
Foam	3.35 ± 0.09	3.38 ± 0.18	4.60 ± 0.27
Foam-resin	4.03 ± 0.15	4.19 ± 0.12	5.29 ± 0.24

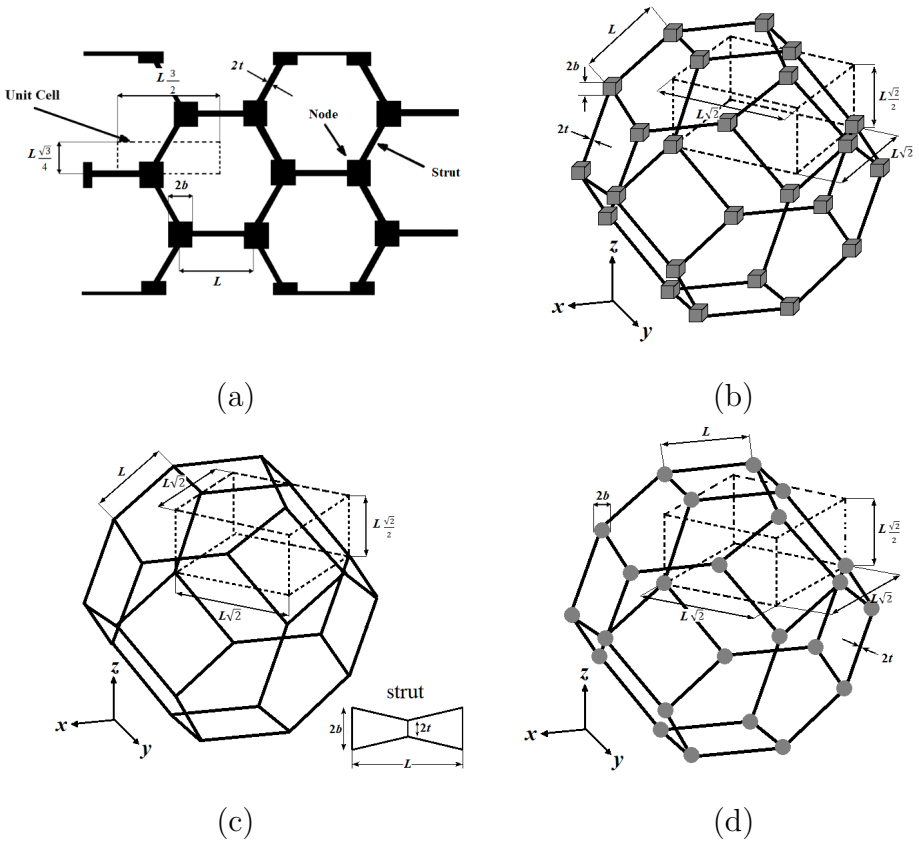

Figure 14: (a) Hexagonal structure and unit cell of Clamidi and Mahajan [8] model. Tetrakaidecahedron cell of (b) Boomsma and Poulikakos [33], (c) Yang (the variation of the strut cross-section on the lower-right side) [35] and (d) Yao [20] models. Dashed hexahedra represent unit cell control volumes for one-sixteenth of the tetrakaidecahedron.

$$\lambda_{foam} = \frac{\sqrt{3}}{2}\left(\frac{rd}{\lambda_f + (1+d)\frac{\lambda_s - \lambda_f}{3}} + \frac{(1-r)d}{\lambda_f + \frac{2d}{3}(\lambda_s - \lambda_f)} + \frac{\frac{\sqrt{3}}{2} - d}{\lambda_f + \frac{4rd}{3\sqrt{3}}(\lambda_s - \lambda_f)}\right)^{-1} \quad (6a)$$

where $r = \frac{t}{b}$ is related to the ratio d which is the dimensionless node thickness given by the following equation:

$$d = \frac{-r + \sqrt{r^2 + \frac{2}{\sqrt{3}}(1-\varepsilon)\big(2 - r(1+\frac{4}{\sqrt{3}})\big)}}{\frac{2}{3}\big(2 - r(1+\frac{4}{\sqrt{3}})\big)} \tag{6b}$$

The authors recommended setting $r = 0.09$ to predict the TC of the foam with 3 % deviation from experimental values.

Boomsma and Poulikakos [33] developed one of the first 3-D tetrakaidecahedron cell heat conduction model illustrated in Figure 14(b) to calculate the TC of a highly porous metal foam by ignoring the contributions from natural convection and thermal radiation:

$$\lambda_{eff} = \frac{\sqrt{2}}{2(R_A + R_B + R_C + R_D)} \tag{7a}$$

where R_A, R_B, R_C, R_D are defined as:

$$R_A = \frac{4d}{\big(2e^2 + \pi d(1-e)\big)\lambda_s + \big(4 - 2e^2 - \pi d(1-e)\big)\lambda_f} \tag{7b}$$

$$R_B = \frac{(e-2d)^2}{(e-2d)e^2\lambda_s + \big(2e - 4d - (e-2d)e^2\big)\lambda_f} \tag{7c}$$

$$R_C = \frac{(\sqrt{2}-2e)^2}{2\pi d^2(1-2e\sqrt{2})\lambda_s + 2\big(\sqrt{2} - 2e - \pi d^2(1-2e\sqrt{2})\big)\lambda_f} \tag{7d}$$

$$R_D = \frac{2e}{e^2\lambda_s + (4-e^2)\lambda_f} \tag{7e}$$

where d is dimensionless foam strut thickness defined as:

$$d = \left(\frac{\sqrt{2}\big(2 - (5/8)e^3\sqrt{2} - 2\varepsilon\big)}{\pi(3 - 4e\sqrt{2} - e)} \right)^{\frac{1}{2}} \tag{7f}$$

and $e = \frac{b}{L}$ is the dimensionless ratio of the edge length of the cubic node to the node-to-node distance. Choosing $e = 0.339$, the difference between the TC value calculated with this model and the experimental value may be as large as 72 %. In order to improve the model, Dai et. al. [34] introduced a modification of Boomsma-Poulikakos model taking the strut orientation into account which presented the new definition of d and R_C as:

$$d = \left(\frac{\sqrt{2}\big(2 - (3/4)e^3\sqrt{2} - 2\varepsilon\big)}{\pi(3 - 2e\sqrt{2} - e)} \right)^{\frac{1}{2}} \tag{8a}$$

$$R_C = \frac{2(\sqrt{2} - 2e)}{\sqrt{2}\pi d^2\lambda_s + 2(2 - \sqrt{2}\pi d^2)\lambda_f} \tag{8b}$$

The best agreement between the predicted and measured values was obtained for $e = 0.198$ with an average deviation of 10 %.

Yang et al. [35] proposed a tetrakaidecahedron cell consisting of square cross-sectioned struts with length L shown in Figure 14(c) under the assumption of parallel heat conduction flow along the highly tortuous cell struts and saturating fluid. The thickness of struts varies between $2t$ in the middle and $2b$ in both ends which equals to the node thickness:

$$\lambda_{foam} = \frac{(1-\varepsilon)\lambda_s}{(1-e+\frac{3e}{2\alpha})\big(3(1-e)+\frac{3}{2}\alpha e\big)} + \lambda_f \varepsilon \tag{9}$$

where $\alpha = \left(\frac{b}{t}\right)^2$ is the ratio of cuboid node to strut cross-sectional area and $e = \frac{2b}{L}$ is the ratio of the node thickness to the node-to-node distance. Assigning $\alpha = 1.5$ and $e = 0.3$ provides the best agreement with an average deviation of 8 % between the model and the experimental results.

Yao et. al. [20] developed a model taking into account the effect of embedding medium and strut orientation and under assumption of Kelvin tetrakaidecahedron cell illustrated in Figure 14(d) assuming that the struts section is triangular. The TC is given by equation:

$$\lambda_{foam} = \big(\frac{\gamma}{\lambda_A} + \frac{1-2\gamma}{\lambda_B} + \frac{\gamma}{\lambda_C}\big)^{-1} \tag{10a}$$

where λ_A, λ_B and λ_C are defined as:

$$\lambda_A = \frac{5\sqrt{2}}{27}\pi\gamma(3-4\gamma)\lambda_s + \big(1 - \frac{5\sqrt{2}}{27}\pi\gamma(3-4\gamma)\big)\lambda_f \tag{10b}$$

$$\lambda_B = \frac{5\sqrt{2}}{9}\pi\gamma^2\lambda_s + \big(1 - \frac{10\sqrt{2}}{9}\pi\gamma^2\big)\lambda_f \tag{10c}$$

$$\lambda_C = \frac{5\sqrt{2}}{27}\pi\gamma^2\lambda_s + \big(1 - \frac{5\sqrt{2}}{27}\pi\gamma^2\big)\lambda_f \tag{10d}$$

where $\gamma = \frac{b}{L}$. The author recommended evaluating gamma from the porosity using Eq. 10e to get the TC with an average deviation of 8 % compared to the experiment.

$$\varepsilon = 1 - \frac{5\sqrt{2}}{9}\pi\gamma^2(3 - 5\gamma) \tag{10e}$$

Firstly, the foam TC is calculated using the above five analytical models and taking into account the geometrical parameters obtained from tomography. The results are plotted in Figure 15(a) and (b) for aluminium foam with air and that embedded in the epoxy resin respectively. The uncertainties in the values of TC are due to the uncertainties of geometrical parameters given in Table 3 and porosities. Secondly, values of foam TC are calculated using the same models but using the recommended fitted parameters proposed by the original authors. In this case, the uncertainty is due to the measured value of porosity only.

6. Discussion

In the case of foam embedded in the epoxy resin (Figure 15(b)), the heat transfer depends only on the conduction mechanism in the two solid phases. The values from analytical models taking into account the fitted parameters by authors are in good agreement with the experiment. However, the analytical models considering sets of parameters defined by the real geometrical characteristics do not estimate proper values except for Yang's model [35]. It is because Yang's model takes the strut cross-section changes into

account, describing the real geometry more accurately. Therefore, considering the real geometry of the foam plays an important role in predicting TC values matching with experiments. This is why the TC values obtained from FE calculations performed on the 3-D geometry of the foams are in good agreement with experiments.

In the case of foam with air, good agreement has been found between the experimental measuremnet and the predicted TC values from the analytical models using the recommended fitted parameters (Figure 15(a)). It proves that under the experimental approach, using GHPA leads to the measurement of the conduction part of the foam TC. Similarly to the previous case, only Yang's model estimates a TC value that is close to the experiment. In addition, the TC value obtained from FE calculation based on the real 3-D geometry from X-ray tomography is also in pretty good agreement with experiment.

7. Conclusion

In the scope of this paper, experimental and FE investigations were conducted to evaluate the conduction part of the TC of an open-cell aluminium alloy foam block. The FE model was developed based on the 3-D image of the stochastic architecture obtained by X-ray tomography. In an alternative approach, the TC values of the foams with air and those embedded in the epoxy resin were evaluated experimentally measuring the thermal resistance of samples with various thicknesses. The adopted GHPA method was used so that the average temperature remains below 30 °C to prevent thermal radiation. The agreement between the results from FE and experiments for

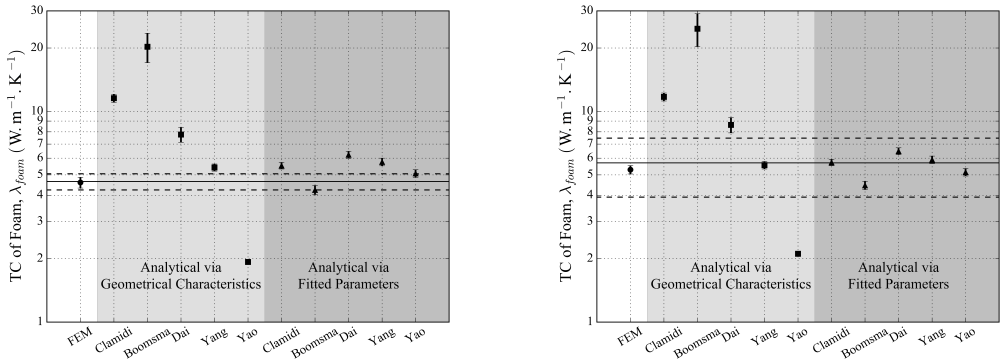

(a) (b)

Figure 15: Comparison between the TC of the foam (a) with air and (b) embedded in epoxy resin, evaluated by experimental, FE and five analytical approaches. Square markers correspond to the analytical results based on geometrical characteristics of the foam and triangle markers to those on the recommended fitted parameters by authors. Solid lines correspond to the measured experimental values and dashed lines to the uncertainties.

the foam embedded in the epoxy resin validates the rest of the results for the foam with air.

Analytical approaches can be easily established knowing the values of porosity and geometrical parameters. However, they do not estimate the value of TC accurately. Previous researchers had to use fitted parameters to get values in agreement with experimental measurements. The FE analysis requires the description of 3-D geometry obtained from X-ray tomography and gives the valid TC value without any fitting parameters. This method is used for the first time, to estimate the TC value of the foam. Moreover, this method could be used to simulate the convection flows through the foam, predicting mechanical and electrical properties in order to optimise materials design.

Acknowledgement

The authors acknowledge the financial support of this study from laboratory MATEIS in France and JSPS Core-to-Core Program in Japan. The authors would like to thank Jérôme Adrien and Joël Lachambre for their help and advises about using X-ray tomography.

References

References

[1] P. Hu, J. Yao, Z. Chen, Analysis for composite zeolite/foam aluminum–water mass recovery adsorption refrigeration system driven by engine exhaust heat, Energy Convers. Manage. 50 (2) (2009) 255–261. doi:10.1016/j.enconman.2008.09.022.

[2] C. Y. Zhao, W. Lu, Y. Tian, Heat transfer enhancement for thermal energy storage using metal foams embedded within phase change materials (PCMs), Sol. Energy 84 (8) (2010) 1402–1412. doi:10.1016/j.solener.2010.04.022.

[3] H. Zhu, B. V. Sankar, R. T. Haftka, S. Venkataraman, M. Blosser, Optimization of functionally graded metallic foam insulation under transient heat transfer conditions, Struct. Multidiscipl. Optim. 28 (5) (2004) 349–355. doi:10.1007/s00158-004-0463-3.

[4] M. Alvarez-Lainez, M. A. Rodriguez-Perez, J. A. de Saja, Thermal conductivity of open-cell polyolefin foams, J. Polym. Sci., Part B: Polym. Phys. 46 (2) (2008) 212–221. doi:10.1002/polb.21358.

[5] A. Bhattacharya, V. V. Calmidi, R. L. Mahajan, Thermophysical properties of high porosity metal foams, Int. J. Heat Mass Transfer 45 (5) (2002) 1017–1031. doi:10.1016/S0017-9310(01)00220-4.

[6] R. Singh, H. S. Kasana, Computational aspects of effective thermal conductivity of highly porous metal foams, Appl. Therm. Eng. 24 (13) (2004) 1841–1849. doi:10.1016/j.applthermaleng.2003.12.011.

[7] J. W. Paek, B. H. Kang, S. Y. Kim, J. M. Hyun, Effective thermal conductivity and permeability of aluminum foam materials, Int. J. Thermophys. 21 (2) (2000) 453–464. doi:10.1023/A:1006643815323.

[8] V. V. Calmidi, R. L. Mahajan, The effective thermal conductivity of high porosity fibrous metal foams, J. Heat Transfer 121 (2) (1999) 466. doi:10.1115/1.2826001.

[9] C. Y. Zhao, T. J. Lu, H. P. Hodson, J. D. Jackson, The temperature dependence of effective thermal conductivity of open-celled steel alloy foams, Mater. Sci. Eng., Proc. Conf. 367 (1-2) (2004) 123–131. doi:10.1016/j.msea.2003.10.241.

[10] C. Y. Zhao, T. J. Lu, H. P. Hodson, Natural convection in metal foams with open cells, Int. J. Heat Mass Transfer 48 (12) (2005) 2452–2463. doi:10.1016/j.ijheatmasstransfer.2005.01.002.

[11] M. Wang, N. Pan, Modeling and prediction of the effective thermal conductivity of random open-cell porous foams, Int. J. Heat Mass Transfer 51 (5-6) (2008) 1325–1331. doi:10.1016/j.ijheatmasstransfer.2007.11.031.

[12] C. Y. Zhao, T. J. Lu, H. P. Hodson, Thermal radiation in ultralight metal foams with open cells, Int. J. Heat Mass Transfer 47 (14-16) (2004) 2927–2939. doi:10.1016/j.ijheatmasstransfer.2004.03.006.

[13] C. Y. Zhao, S. A. Tassou, T. J. Lu, Analytical considerations of thermal radiation in cellular metal foams with open cells, Int. J. Heat Mass Transfer 51 (3-4) (2008) 929–940. doi:10.1016/j.ijheatmasstransfer.2007.10.010.

[14] N. Dukhan, P. D. Quiñones-Ramos, E. Cruz-Ruiz, M. Vélez-Reyes, E. P. Scott, One-dimensional heat transfer analysis in open-cell 10-ppi metal foam, Int. J. Heat Mass Transfer 48 (25-26) (2005) 5112–5120. doi:10.1016/j.ijheatmasstransfer.2005.07.012.

[15] K. Boomsma, D. Poulikakos, F. Zwick, Metal foams as compact high performance heat exchangers, Mech. Mater. 35 (12) (2003) 1161–1176. doi:10.1016/j.mechmat.2003.02.001.

[16] E. Maire, X-ray tomography applied to the characterization of highly porous materials, Annu. Rev. Mater. Res. 42 (2012) 163–178. doi:10.1146/annurev-matsci-070511-155106.

[17] E. Maire, P. J. Withers, Quantitative x-ray tomography, Int. Mater. Rev. 59 (1) (2014) 1–43. doi:10.1179/1743280413Y.0000000023.

[18] G. T. Herman, Fundamentals of computerized tomography: image reconstruction from projections, Springer Science & Business Media, 2009.

[19] W. C. Thomas, R. R. Zarr, Thermal response simulation for tuning PID

controllers in a 1016 mm guarded hot plate apparatus, ISA Trans. 50 (3) (2011) 504–512. doi:10.1016/j.isatra.2011.02.001.

[20] Y. Yao, H. Wu, Z. Liu, A new prediction model for the effective thermal conductivity of high porosity open-cell metal foams, Int. J. Therm. Sci. 97 (2015) 56–67. doi:10.1016/j.ijthermalsci.2015.06.008.

[21] M. A. A. Mendes, S. Ray, D. Trimis, Evaluation of effective thermal conductivity of porous foams in presence of arbitrary working fluid, Int. J. Therm. Sci. 79 (2014) 260–265. doi:10.1016/j.ijthermalsci.2014.01.009.

[22] B. Choi, I. Yeo, J. Lee, W. K. Kang, T. Song, Pillar-supported vacuum insulation panel with multi-layered filler material, Int. J. Heat Mass Transfer 102 (2016) 902–910. doi:10.1016/j.ijheatmasstransfer.2016.06.032.

[23] M. Q. Brewster, Thermal radiative transfer and properties, Wiley, 1992.

[24] M. F. Modest, Radiative Heat Transfer, Elsevier Science, Oxford, 2013.

[25] C. Petit, S. Meille, E. Maire, Cellular solids studied by x-ray tomography and finite element modeling–a review, J. Mater. Res. 28 (17) (2013) 2191–2201. doi:10.1023/A:1006643815323.

[26] O. Caty, E. Maire, S. Youssef, R. Bouchet, Modeling the properties of closed-cell cellular materials from tomography images using finite shell elements, Acta Mater. 56 (19) (2008) 5524–5534. doi:10.1016/j.actamat.2008.07.023.

[27] Abaqus version 6.13 documentation collection (2013).

[28] E. Andrews, W. Sanders, L. J. Gibson, Compressive and tensile behaviour of aluminum foams, Mater. Sci. Eng., A 270 (2) (1999) 113–124. doi:10.1016/S0921-5093(99)00170-7.

[29] A. P. Roberts, E. J. Garboczi, Computation of the linear elastic properties of random porous materials with a wide variety of microstructure, Proc. R. Soc. London, Ser.A 458 (2021) (2002) 1033–1054. doi:10.1098/rspa.2001.0900.

[30] Avizo® 8 user's guide (2014).

[31] S. Youssef, E. Maire, R. Gaertner, Finite element modelling of the actual structure of cellular materials determined by X-ray tomography, Acta Mater. 53 (3) (2005) 719–730. doi:10.1016/j.actamat.2004.10.024.

[32] Y. Amani, A. Öchsner, Finite element simulation of arrays of hollow sphere structures, Materialwiss. Werkstofftech. 46 (4-5) (2015) 462–476. doi:10.1002/mawe.201500422.

[33] K. Boomsma, D. Poulikakos, On the effective thermal conductivity of a three-dimensionally structured fluid-saturated metal foam, Int. J. Heat Mass Transfer 44 (4) (2001) 827–836. doi:10.1016/S0017-9310(00)00123-X.

[34] Z. Dai, K. Nawaz, Y. G. Park, J. Bock, A. M. Jacobi, Correcting and extending the Boomsma–Poulikakos effective thermal conductivity model for three-dimensional, fluid-saturated metal foams, Int. Commun. Heat Mass Transfer 37 (6) (2010) 575–580. doi:10.1016/j.icheatmasstransfer.2010.01.015.

[35] X. H. Yang, J. X. Bai, H. B. Yan, J. J. Kuang, T. J. Lu, T. Kim, An analytical unit cell model for the effective thermal conductivity of high porosity open-cell metal foams, Transp. Porous Media 102 (3) (2014) 403–426. doi:10.1007/s11242-014-0281-z.

[36] D. Baillis, R. Coquard, S. Cunsolo, Effective conductivity of Voronois closed-and open-cell foams: analytical laws and numerical results, J. Mater. Sci. 52 (19) (2017) 11146–11167. doi:10.1007/s10853-017-1226-z.